HHS Public Access

Author manuscript

J Neural Eng. Author manuscript; available in PMC 2016 June 06.

Published in final edited form as:

J Neural Eng. 2016 April ; 13(2): 026030. doi:10.1088/1741-2560/13/2/026030.

A low-cost, multiplexed μECoG system for high-density recordings in freely-moving rodents

Michele Insanally[#1,2], **Michael Trumpis**[#3,4], **Charles Wang**[3,4], **Chia-Han Chiang**[3,4], **Virginia Woods**[3,4], **Kay Palopoli-Trojani**[4], **Silvia Bossi**[4,5,6], **Robert C. Froemke**[1,2], and **Jonathan Viventi**[3,4,*]

[1]Skirball Institute for Biomolecular Medicine, Neuroscience Institute, Departments of Otolaryngology, Neuroscience and Physiology, New York University School of Medicine, New York, NY, USA

[2] Center for Neural Science, New York University, New York, NY, USA

[3] Polytechnic Institute of New York University, Department of Electrical and Computer Engineering, New York, NY, USA

[4] Department of Biomedical Engineering, Duke University, Durham, NC, USA

[5] Robotics Laboratory, C.R. Casaccia, ENEA, V. Anguillarese, 301, 00123 S. Maria di Galeria, Roma, Italy

[6]BioRobotics Institute, Scuola Superiore Sant'Anna, Viale Rinaldo Piaggio 34, 56025 Pontedera, Italy

[#] These authors contributed equally to this work.

Abstract

Objective—Micro-electrocorticography (μECoG) offers a minimally invasive neural interface with high spatial resolution over large areas of cortex. However, electrode arrays with many contacts that are individually wired to external recording systems are cumbersome and make recordings in freely-behaving rodents challenging. We report a novel high-density 60-electrode system for μECoG recording in freely-moving rats.

Approach—Multiplexed headstages overcome the problem of wiring complexity by combining signals from many electrodes to a smaller number of connections We have developed a low-cost, multiplexed recording system with 60 contacts at 406 μm spacing. We characterized the quality of the electrode signals using multiple metrics that tracked spatial variation, evoked-response detectability, and decoding value. Performance of the system was validated both in anesthetized animals and freely-moving awake animals.

Main results—We recorded μECoG signals over the primary auditory cortex, measuring responses to acoustic stimuli across all channels. Single-trial responses had high signal-to-noise ratios (up to 25 dB under anesthesia), and were used to rapidly measure network topography within ~10 seconds by constructing all single-channel receptive fields in parallel. We characterized

[*]To whom correspondence should be addressed. ; Email: j.viventi@duke.edu

evoked potential amplitudes and spatial correlations across the array in the anesthetized and awake animals. Recording quality in awake animals was stable for at least 30 days. Finally, we used these responses to accurately decode auditory stimuli on single trials.

Significance—This study introduces (1) a μECoG recording system based on practical hardware design and (2) a rigorous analytical method for characterizing the signal characteristics of μECoG electrode arrays. This methodology can be applied to evaluate the fidelity and lifetime of any μECoG electrode array. Our μECoG-based recording system is accessible and will be useful for studies of perception and decision-making in rodents, particularly over the entire time course of behavioral training and learning.

1. Introduction

The ability to record stable cortical surface potentials using microelectrode arrays is essential for investigating questions related to perceptual learning and the mechanisms underlying behavioral improvements with neuroprosthetic devices. Miniaturized micro-electrocorticography (μECoG) has emerged as an important class of implantable electrodes capable of recording cortical-surface field potential at mesoscopic scales [1,2]. μECoG combines high spatial and temporal bandwidth, capturing fine-scale structure lost to EEG, ECoG, and fMRI, and can be scaled to cover larger areas than intracortical microelectrode arrays. The microfabrication methods used to construct μECoG electrodes have enabled investigative tools at a very wide range of sizes, from extensive coverage of multiple cortical areas in nonhuman primates [3,4] to coverage matched to the size and density of cortical neurons in rats [5]. Compact, high-density arrays are well suited for recording at the scale of rodent cortical systems, allowing customized coverage of multiple areas [6–9].

However, μECoG arrays that interface with large areas of the cortical surface in rodents at high spatial resolution require dozens to hundreds of electrodes. Obtaining recordings from freely behaving animals with a large number of electrode contacts is challenging and expensive, which limits the number of animals that can be simultaneously monitored. Furthermore, the thin-film circuit materials and fabrication techniques that have resulted in novel electrode arrays require advanced lithography and/or cleanroom facilities [10–14]. As a result, these devices remain largely inaccessible to the majority of experimentalists. To overcome these limitations, we have developed a low-cost, multiplexed, integrated μECoG system based on commercial electronics and flexible printed circuit board (flex-PCB) fabrication. By leveraging mass-production processes for flex-PCB fabrication we have developed a high density, flexible array with contacts at sub-millimeter pitch. We have also developed a low-cost, lightweight headstage that multiplexed the numerous electrode channels. The μECoG electrode array costs $29 and the headstage costs $130. The headstage was designed to be head-mountable as part of a chronically implanted system that interfaced with the electrode using a low profile, high density, and solder-free connector. The high channel-count recordings were evaluated using rigorous analytical methods that measured the clarity and spatial diversity of the array signal in response to acoustic stimuli.

This study highlights a μECoG recording system designed as a ready-made tool for experimental neuroscientists. The low cost of the headstage promotes its feasibility as a

disposable unit for implantation of multiple animals in parallel. We present the design of the recording system, as well as multiple validations of the recording quality from the primary auditory cortex of anesthetized and awake rats over a period of at least one month. Specifically, we used a series of detailed and diverse signal characteristics such as spatial correlation profiles, power spectral densities, RMS voltage, multivariate waveform amplitude, signal to noise ratios, frequency response areas, topographical maps, single-trial voltage heat maps, and single-trial decoding to determine the stability and reliability of *in vivo* μECoG recordings.

2. Methods

2.1. Electrode array fabrication

We designed a flexible μECoG array with 61 passive electrodes spaced 406 μm apart (figure 1(a)) [15]. The arrays were fabricated using the following standard flexible printed circuit board processing techniques by Microconnex Flex Circuits (Snoqualmie, WA). Each electrode contact was 203 μm in diameter. A 12 μm thick polyimide sheet, covered on both sides with 5 μm of copper formed the core of the device (AP7408EJ 5-12-5). Electrode pads, wires and connector pads were patterned and etched into the top copper layer. In order to increase the flexibility of the final device, the bottom copper layer was not used and etched away. A 15 μm layer of liquid photoimageable solder mask (Taiyo PSR-9000, Taiyo America) was deposited on the surface of the array and patterned. Exposed copper electrode pads forming the electrodes and connector pads were finished with electroless nickel immersion gold (figure 1(a) inset). Five holes were laser-cut into the array, each 305 μm in diameter, to provide windows for simultaneous unit recording with penetrating electrodes, or to monitor the depth of penetration of surface stimulation. Each of the 61 electrodes was individually wired with 25 μm wires spaced at 25 μm, which minimized the width of the array to 3.4 mm where it must exit the skull and scalp. These traces fanned out slightly (14.5 mm) to exposed pads designed to mate with a high-density (200 μm pitch) zero insertion force (ZIF) connector with 61-pins (HiRose, Inc). The ZIF connector had a low profile and did not require soldering to connect with the flex-PCB array. FR4 material was added as a stiffener over the connection area to reach the recommended thickness (200 μm) for the ZIF connector to mate properly with the flexible circuit.

The average electrode impedance was 26.4±1.7 kΩ at 1 kHz (Supplemental figure 2a), providing low noise sensing of field potentials. The electrodes were arranged in an 8 × 8 grid, covering 10.6 mm^2. Three corner electrodes were omitted. The fourth corner electrode was intentionally unexposed to serve as a test for the resistance of the encapsulation in awake experiments, reducing the number of active recorded sites to 60. Consequently, this electrode was omitted from the design of the recording headstage.

2.2. Analog multiplexed headstage

We designed a headstage for use with the flex-PCB electrode that provided amplification and multiplexing of signals from the 60 recorded channels (figure 1(b)). The headstage was constructed from off-the-shelf integrated circuits and specifications suitable for inexpensive PCB manufacturing and assembly. The headstage was based on our previous design [16], but

with improved signal to noise characteristics, signal quality, and reduced size. Electrode contacts were routed from the ZIF connector to 30 dual op-amps in a unity gain configuration (OPA2376, Texas Instruments). The 60 outputs of these buffers were multiplexed by a pair of dual 16:1 multiplexers (ADG726, Analog Devices, Inc). The outputs of the multiplexers were high-pass filtered at 0.0016 Hz to remove the average electrode DC offset and subsequently amplified by a pair of dual op-amps with 20× gain (OPA2376, Texas Instruments). The gain value we chose provided a large input voltage dynamic range (±125 mV), while reducing noise in the analog transmission of multiplexed signals to the analog to digital converters. All signal and interface wires were carried by an ultra-flexible μHDMI cable (Draco Electronics, LLC, CA, US) with analog signals measured differentially on the shielded, twisted pairs. The headstage had a height profile of < 27 mm and weighed < 3 g, making it suitable for awake, *in vivo* recording in a freely-moving animal.

2.2.1 Acquisition interface PCB—We interfaced our headstage with National Instruments data acquisition systems using a custom interface PCB that provided regulated power and converted the multiplexer command signals from 5V to 2.5V logic (figure 1(c)). A low-noise bi-polar supply for the multiplexed headstage was generated by first inverting the 5V onboard power from the NI system to −5V using a charge pump voltage inverter (TPS60403DBVR, Texas Instruments) and then using a pair of ultra-low noise positive and negative linear regulators to provide regulated ±2.5V (TPS7A4901DGNR and TPS7A3001DGNR, Texas Instruments). The interface PCB was connected to a multicard PXI system (PXI-1033 or PXIe-1073, National Instruments) with 18-bit analog to digital converter cards (PXI-6289). However, a USB-6289 or any M-series or X-series DAQ system would also be compatible. Custom LabVIEW data acquisition software was used to control the acquisition and perform real-time demultiplexing, display and recording. We have previously published this software with an open source license [17].

2.3. Surgical procedure for anesthetized and awake recordings in rodents

All animal procedures were performed in accordance with National Institutes of Health standards and were conducted under a protocol approved by the New York University School of Medicine Institutional Animal Care and Use Committee. A specific surgical protocol was developed for implantation of this device in rats. Experiments were carried out in a sound-attenuation chamber. Ten male Sprague-Dawley rats 4-6 months old were anesthetized with ketamine (40 mg/kg, intramuscular injection.) and dexmedetomidine (0.125 mg/kg, intramuscular injection) or pentobarbital (50 mg/kg, intraperitoneal injection). The head was secured in a custom head-holder that left the ears unobstructed. A longitudinal incision was made along the midline to expose the skull. Five bone screws were inserted into the skull around the point of entry of the electrode array to help anchor the dental cement (C & B Metabond Quick! Luting Cement) pedestal to the skull. After reflecting the right temporalis muscle, a 5 mm × 5 mm craniotomy was made on the right temporal skull to expose the brain and a sterilized electrode array was subdurally or epidurally placed over core auditory cortex using vasculature landmarks. For the recovery procedure, the craniotomy was then covered with a 1.5% solution of warm agarose. After the agarose solidified, the craniotomy was encapsulated with industrial grade cement (Grip Cement,

Dentsply Caulk). After the craniotomy was covered and the array was secure, a thin silver wire was soldered between the headstage and the skull screws to be used as ground and reference. Finally, the entire headstage, reference wire and skull screws were then encapsulated in industrial grade cement. The surgical site was flushed with a povidone-iodine (Betadine) solution and the incision points sutured. Animals were left to fully recover before electrophysiological recordings were made approximately one week later. One animal was implanted with our first version headstage [16], while the second animal was implanted with our improved second version headstage, described above. For acute implantation, the craniotomy procedure was performed as described above, except it was left uncovered and irrigated with sterile saline during the recording session.

2.4. Electrophysiological recording and stimulus presentation

Responses to tone pips of 13 frequencies (0.5-32 kHz, 0.5 octave spacing, 50 ms in duration, 2 ms cosine-squared ramps) at 8 sound pressure levels (SPLs, 0-70 dB SPL, 10 dB SPL steps) were recorded to reconstruct frequency-intensity response areas. Pure tones were presented in a pseudorandom sequence at a rate of 1.25 Hz, to the contralateral ear (for acute experiments) using a calibrated free-field speaker (MF1 Multi-Field Magnetic Speaker, Tucker-Davis Technologies). Each tone was repeated 30 times for each dB SPL played. Responses to brief broadband click stimuli (0.2 ms in duration, 70 dB SPL, 1.25 Hz, 250 repetitions) were also recorded for three awake sessions with one rat (days 30, 37, 56) and all awake sessions with another rat. Acoustic stimuli were generated using an auditory processor (TDT System III RZ6). The speaker was calibrated to have <1% harmonic distortion and flat output in the frequency range used.

2.5. Data acquisition

The multiplexer outputs were sampled at 250 kHz with an oversampling factor of 8 on two PXI-6289 data acquisition cards, yielding a multiplexer switching rate of 31,250 Hz. Samples taken before the multiplexer output had completely settled to 18-bit accuracy were discarded. The remaining samples were averaged to reduce noise, yielding an effective final sampling rate of 1,953 Hz per electrode channel.

2.6. Neural signal analysis

Electrode sites from each recording were first screened based on signal power. All sites with background RMS voltage between $20\ \mu V < p < 300\ \mu V$ were included for analysis. Power less than $20\ \mu V$ corresponded with pre-amplifier saturation, while power greater than $300\ \mu V$ consistently indicated intermittent corruption from non-neural sources.

2.6.1. Power spectral density—Spectral density functions were estimated for 600-millisecond segments of interstimulus baseline μECoG using Thomson's multitaper estimator, which is the mean of approximately uncorrelated spectral estimators computed using orthonormal tapers [18,19]. We used 6 Slepian tapers with a time-bandwidth product of 3.5 and a spectral resolution of 11.67 Hz. The power spectral density functions were averaged first over segments and then over electrode channels for a final stationary estimate.

2.6.2. Analysis of evoked responses—For visualization and analysis of evoked responses, timeseries were bandpass filtered to 2-100 Hz using a digital zero-phase 6th order Butterworth filter. Evoked-responses were measured using the middle latency response windowed over a 50 ms period after stimulus onset. We scored response waveforms in a feature-independent manner using a generalized, unit-less vector magnitude called the Mahalanobis distance [20_24]. A center (mean) vector μ and covariance matrix Σ were estimated from 50 ms windows of all inter-stimulus baseline periods, and the squared-length of each evoked response vector r was was calculated as

$$d^2(r) = (r-\mu)^T \Sigma^{-1} (r-\mu).$$

Defined this way, the Mahalanobis distance is a fully multivariate measure of the divergence between an evoked response and the spontaneous activity of the baseline process; under a Gaussian interpretation it can be read as the length of a vector of standardized scores. However, it is challenging to calculate the Mahalanobis distance in high dimension because the covariance matrix is difficult to estimate with precision, and may be numerically ill-conditioned. To address this, we regularized the covariance estimator by using a convex combination of the sample covariance estimator and the identity. The resulting estimator has superior asymptotic consistency and provides a numerically well-conditioned matrix [25].

The Mahalanobis distance was also used to assess a signal-to-noise ratio. In one sense, the score automatically normalizes the response with respect to baseline since the distance is calculated over a space where the baseline process is isotropic white noise by design. However, we defined an evoked-signal-to-noise ratio (evoked SNR) that normalized the response strength by an empirical measure of the baseline variance:

$$\sigma^2_{\mathscr{B}} = exp\left\{ |\mathscr{B}|^{-1} \sum\nolimits_{b \in \mathscr{B}} ln \quad d^2(b) \right\}.$$

The logarithm was used as a variance-stabilizing transform. The response strength s_i^2 for the i^{th} tone was defined identically to the baseline variance for the corresponding set $\mathscr{T}_i$ of replicated middle latency responses, and the evoked SNR was taken as the largest response strength divided by the baseline variance:

$$\text{Evoked SNR} = \max_i \left\{ s_i^2 \right\} / \sigma^2_{\mathscr{B}}.$$

Evoked SNR and peak-to-peak amplitude were only measured for channels in which the RMS voltage of trial-averaged post-stimulus activity could be reliably distinguished from that of trial-averaged pre-stimulus activity. The mean and variance of a lognormal distribution of trial-averaged pre-stimulus power was estimated by bootstrapped replicates. If the trial-averaged post-stimulus power for any condition scored at the 99th percentile of the estimated pre-stimulus power distribution, the channel was deemed responsive.

2.6.3. Estimation of best frequency—Best frequency was estimated by computing the center of mass of the response scores at 70 dB SPL. The response score mass function was defined over a circular domain of tones in order to prevent biasing the center of mass towards the interior of the 0.5-32 kHz stimulus range. Frequency response areas from anesthetized and awake recordings were also constructed to further validate the recording system for auditory cortical recordings (Supplemental figure 1).

2.6.4. Spatial characteristic of site-site correlation—A Pearson correlation coefficient was computed for μECoG signal between all pairs of electrode channels. For each pair, correlation coefficients were computed for and averaged over 600 millisecond blocks of 10-100 Hz bandpassed surface potential from interstimulus windows. We used a descriptive model of exponential decay $\rho(x) = \exp\{-x/\lambda\}$ to quantify the characteristic length of correlation roll-off as a function of site-site distance [26,27]. The characteristic length λ is termed the "e-fold distance", referring to the site-site distance at which correlation is expected to be diminished by a factor of the constant e. Observed correlations were grouped at discrete distances, due to the grid geometry of the electrode array, and exhibited considerable heteroskedasticity between groups. Correlation values were log-transformed, and the model was fit by linear least squares with residuals weighted by the inverse of the within-group variance. The hypothesis test for differences between slopes was based on the Student's t statistic of multiple regression coefficients.

2.6.5. Linear classification scheme—To predict stimulus conditions, a supervised linear classifier was developed consisting of a compressive stage and a discriminative stage [28]. All sites with normal RMS voltage ($20\ \mu V < p < 300\ \mu V$) were included for analysis, resulting in P viable sites. Naive feature vectors were constructed by concatenating all length-M post-stimulus responses from the P responsive sites, resulting in a PM-dimensional vector. Using 6-fold cross-validation, each of the PM variates were first mean/variance normalized. The naive feature vectors in the training set were then compressed using the singular value decomposition (SVD) to obtain a reduced-rank approximation. The optimal rank for each classifier was determined in a separate cross-validated tuning stage using multiple shuffle-and-split cross-validations. Finally, linear discriminant analysis (LDA) was applied to estimate the tone-likelihood map of the resulting compressed feature space. Naive feature vectors from the training set were normalized and compressed according to the learned transformations, and the maximum likelihood tone was estimated for each response. Average accuracy over all tones was estimated by the total proportion of correct predictions. A task-specific measure of prediction error was defined as the spectral distance in octaves between the stimulation tone t and the tone predicted by the decoding function $g(\cdot \mid t)$ from the response r: $e_{r/t} = |\log_2 t - \log_2 g(r \mid t)|$. The average prediction error $\hat{e} = E_t\{E_{r/t}\{e_{r/t}\}\}$ was estimated using the empirical conditional distribution $p(r \mid t)$ given by the decoding confusion matrix. Confidence intervals of the decoding error were estimated by resampling decoder output to create bootstrapped replicates of the confusion matrix.

3. Results

3.1. Anesthetized and awake recordings

We designed, built, and validated a multiplexed μECoG system shown in figure 1 for long-term recordings from rat auditory cortex (figure 1). After implantation, we measured responses to acoustic stimuli from the primary auditory cortex and surrounding auditory areas of ten rats divided into four groups: four rats were implanted subdurally under ketamine anesthesia, two rats were implanted subdurally under pentobarbital anesthesia, three rats were implanted epidurally under ketamine, and two rats that were implanted epidurally were also recorded while awake and freely moving. The tenth rat was implanted epidurally and subsequently subdurally under ketamine. Figure 2 shows continuous activity on all 60 channels from an animal under pentobarbital anesthesia during pure tone presentation. Single-trial tone-evoked responses were visible 10-15 ms after stimulus onset (figure 2(a) and (b)). Evoked responses were frequently visible in real-time on the data acquisition display, sometimes consistently rising > 1 mV above the ongoing signal (figure 6(a)). Figure 3 shows continuous μECoG recordings from an awake animal that was allowed to move freely within the home cage, tethered only by an ultra-flexible μHDMI cable. Although the ratio of evoked power to baseline power was lower in freely-moving animals than in anesthetized animals, single-trial tone-evoked responses were still visible on many electrodes. The headstage did not include a lowpass filter before the multiplexer discretized the voltage signal, but we did not observe any aliasing artifacts, presumably due to the lack of appreciable harmonic content in the neural signal at frequencies above ~900 Hz.

3.2 Signal Characteristics

Power and correlation statistics of the interstimulus baseline were computed for different experimental conditions (figure 4). Signal power from the awake and anesthetized conditions was visibly elevated relative to the system noise floor of 2.1 μV RMS between 1-300 Hz, improved from 5.9 μV RMS in [16]. Low frequency (1-10 Hz) and narrow-band power (100-120 Hz) due to ketamine anesthesia [29] were both evident in the power spectra. For the purpose of comparing signal properties across recording conditions, we restricted our analysis to the 10-100 Hz band that was free of anesthesia-related phenomena.

RMS voltage of the interstimulus baseline was consistent across nine recording sessions spanning 10 weeks in one animal and seven sessions spanning five weeks in a second animal. A linear regression over days with random effects per channel showed no significant trend (figure 4(b), slope=0.01 μV/day, $p>0.05$, likelihood ratio test with 1 degree of freedom) indicating that the recording system was stable.

In order to monitor signal redundancy across channels, we measured the spatial correlation between channels by computing the Pearson correlation coefficient between all pairs of electrode channels (figure 4(c)). The spatial correlation functions were well-described by a standard exponential covariance model for random fields (see Methods for details on the calculation and model fitting for spatial correlation). In figure 4(c), we compared the correlation decay for the four recording conditions. The random fields from anesthetized subdural recordings (ketamine and pentobarbital) were least correlated on remote sites (e-

fold constants were λ =2.5 mm for both conditions, $p>0.05$, Student's t-test). The e-fold distance was significantly higher for epidural recordings (λ =4.4 mm, $p<0.001$, Student's t-test). Two representative subdural and epidural recordings from the same ketamine-anesthetized animal showed a consistent increase in e-fold distance from 2.5 mm to 4.3 mm ($p<0.001$, Student's t-test). This increase in the characteristic length of correlation might be due to the lateral spread of current across the cerebrospinal fluid and the *dura mater*. The e-fold distance was even larger for awake recordings (figure 4(c), λ = 13.9 mm, $p<0.001$, Student's t-test).

To track the random field characteristics of the implanted electrodes, we monitored the spatial correlation of each implanted animal over recording sessions for a maximum of 73 days post-implantation (figure 4(d)). The spatial constant of correlation gradually increased to a final level of 14.3 mm after day 73 in animal one, but dramatically increased to levels between 60.2-103.1 mm after day 15 in animal two. The rising e-folding distance was consistent with the possibility of a growing number of sites becoming electrically coupled. An accelerated lifetime study (Supplemental figure 2b) predicted stable impedances over ~1 month at body temperature.

3.3 Tonotopic organization and high trial-to-trial reliability

We recorded responses to a combination of pure tone pips (0.5-32 kHz) at varying intensities (0-70 dB SPL). These responses were used to reconstruct a best frequency map at 70 dB SPL over the entire array (figure 5(a)). Single-trial evoked responses were clearly and reliably distinguishable from baseline activity (figure 5(b-d)). The frequency tuning of electrode sites was apparent in single-trial evoked responses, and was consistent with the tonotopic organization of auditory areas mapped intracortically using spiking activity [30,31].

3.4 Evoked signal to noise ratio for anesthetized and awake in vivo recordings

In order to measure the evoked signal strength relative to background activity we computed the peak-to-peak voltage and the evoked SNR at best frequency recorded at 70 dB SPL (figure 6). The evoked signal power, reflected by peak-to-peak voltage, varied greatly with brain state (anesthetized versus awake), as well as between anesthesia conditions. In the case of ketamine anesthesia, the higher evoked power was correlated with high baseline power, such that the SNR was lower on average than the pentobarbital condition. For 70 dB SPL tones, the median value of evoked SNR across anesthetized conditions was between 6.7-9.6 dB (or 4.7-9.1 times the background level), with a large share of highly responsive sites scoring >12 dB (~16 times the background level). For awake recordings the median evoked SNR was 1.1 dB. The decrease in evoked SNR seen in the awake recordings is expected; significant differences in response properties between anesthetized and awake recordings have been widely reported in the literature [32–35].

3.5 Awake recordings

We used our electrophysiological system to record evoked responses with an epidural electrode array up to 73 days (nine recording sessions) in one rat and six weeks (eight recording sessions) in a second rat. Recordings were made until the stimulus-decoding error

(Section 3.6) was indistinguishable from random choice, which indicated a lack of functionally relevant neural responses. Surface potentials from auditory cortex were recorded while the animals were allowed to move freely within the home cage, tethered only by an ultra-flexible μHDMI cable. We observed consistent responses to the best frequency tone played at 70 dB SPL over the course of 10 weeks. The best frequency response waveforms (in this case at 8 kHz) depicted in figure 7(a) show similar morphology, especially after the first week of implantation (the 36 pairwise Pearson's correlation coefficients were between $-0.55 < \rho < 0.91$, median = 0.51). Examples of response waveforms to click stimuli from the same electrode are shown for days 37 and 56 (figure 7(b)).

The evoked SNR for best frequency responses at 70 dB SPL across awake recording sessions is shown in figure 7(c). During the first awake recording sessions (day 6) the median evoked SNR over sites was 1.3 dB (n=2 rats) and during the last awake recording session (day 73) it was 1.0 dB (n=1). On all 14 post-implant days, the evoked SNR was significantly higher than a control SNR computed with baseline samples (figure 7(c), shown in gray, maximum $p<0.001$, Mann-Whitney U test, one-sided). As an additional response metric we measured the peak-to-peak amplitude for the best frequency responses at 70 dB SPL. On the first awake recording sessions (day 6) the median peak-to-peak amplitude was 106.0 μV (n=2) and on the last awake recording session it was 63.4 μV (n=1). The evoked SNR was also measured for responses to click stimuli from six awake recording sessions (figure 7(d)). Click-evoked SNR appeared more consistent than tone-evoked SNR (the median SNR over sites on day 6 was 1.5 dB (n=2), and on day 56 it was 1.4 dB (n=1)). On all post-implant days, click-evoked SNR was higher than control SNR (maximum $p<0.001$, Mann-Whitney U test, one-sided).

3.6 Tone classification from single-trials

In order to determine if evoked responses could predict tone identity, we trained a linear classifier to predict tones based on the observed pattern of neural activity on single-trials. The mean classification accuracies for different recording conditions were all above chance: 86% and 52% for anesthetized subdural preparations (pentobarbital and ketamine, respectively), 49% for ketamine and epidural, and 29% for awake and epidural recordings (the chance rate for 13 classes was 7.7%). Figure 8(a) depicts examples of confusion matrices and decoding accuracies from the highest-accuracy recording in each group. We also calculated decoding error based on the spectral distance in octaves between actual and predicted tones (figure 8(b)). Mean decoding errors were 0.11 octaves and 0.53 octaves when recording subdurally (under pentobarbital and ketamine respectively), 0.62 octaves for ketamine and epidural recordings, and 1.2 octaves for awake recordings. All decode errors were less than the chance error of 2.2 octaves that would be observed with a uniform confusion matrix. As a measure of stability, we tracked the decode error separately for each implanted animal over a maximum of 73 days (figure 8(c)). The error shows a gradual increase over days in both implants, and the median decoding error per implant was not significantly different ($p>0.05$, Mann-Whitney U test, two sided). We observed amplifier saturation on several channels between days 9-22 in one animal (figure 8(c), shown in black)

that contributed to larger errors. The error level returned to a consistent level at day 30 when all channels were again recorded.

4. Discussion

We validated a low-cost, multiplexed headstage and electrophysiological recording system that directly interfaces with μECoG arrays for high-density recordings *in vivo*. Our system reduced the number of electrode wires required for recording and also had the additional benefit of reduced implant size. While the multiplexing headstage is not significantly smaller than other multiplexed headstages, the low-cost design enables it to be directly implanted on the animal, eliminating an additional electrode adapter PCB to convert from the electrode to an Omnetics connector. Besides reducing the height of the recording system by an additional 12 mm it further reduces the cost of the implantation. In addition, the lightweight design of the headstage (< 3 grams) makes it suitable for recordings in mice, gerbils and other small rodents.

The μECoG electrode was designed to balance low-cost industrial fabrication with the high integration density desired for fine pitch neural interfaces. Flex-PCB fabrication is a practical alternative to other processes utilized in commercially available μECoG arrays. MEMS-fabrication of thin-film electrodes (such as those sold by NeuroNexus [36]) can support features sizes of approximately half the dimension of the flex-PCB process. However, the fabrication process is more cost-intensive than PCB manufacturing: a 64-contact μECoG array with lower electrode density (500 μm pitch) costs $1,365 as compared to $29 for our μECoG array. Laser-fabricated electrode circuits (such as those sold by CorTec) are also available. These devices, patterned from platinum or platinum-iridium foil and encapsulated by medical grade silicone, have improved biocompatibility, but are limited in feature density. Parallel metal wires require redundant empty tracks between metal traces and have an effective pitch of 100 μm [37] reducing the achievable electrode spacing to >1mm, while the total thickness of the arrays are >70 μm [38]. An improved process using picosecond lasers can reduce the effective pitch size to 25 μm [39], however this is not yet commercially available. The Flex-PCB fabrication method we utilized supports track pitches of 50 μm and device thicknesses of ~25 μm.

We demonstrated that our electrophysiological system can be used to record surface potentials *in vivo* for at least one month. While we were able to record for up to 10 weeks in one animal, in a second implanted animal 75% of the channels became highly correlated and likely reflected a wiring failure around the third week of implantation. In addition, our accelerated lifetime experiment (Supplemental figure 2) suggest that the stable lifetime of our μECoG arrays may be limited to ~1 month, after which point over 10% of sites developed high impedance due to damage to the electrode pad or wire trace. While the accelerated lifetime study was consistent with the second implanted animal (stable recordings for one month), it did not correspond with the first implanted animal (stable recordings for 10 weeks), indicating that the *in vitro* results may not accurately predict *in vivo* outcomes and it may be possible to record for longer *in vivo*. We are continuing to investigate new materials for our μECoG arrays that will extend their lifetime.

The μECoG arrays also contain copper as a base metal to form the interconnections and nickel, both of which are not biocompatible. Similarly, the biocompatibility of the soldermask encapsulation used is not known. However, the copper and nickel are protected from the brain by surface gold plating. ECoG arrays fabricated with the same materials have been used successfully in non-human primates [3]. To solve this limitation, we are developing new μECoG devices that contain only noble metals and encapsulation materials with known biocompatibility.

Decoding performance measured in awake animals remained above chance up to 73 days post-implantation in animal one, and up to 45 days in animal two (figure 8(c)). The variance in decoding performance seen in days post-implant (figure 8(c)), shown in black) is likely not explained by the minor fluctuations in evoked SNR and peak-to-peak values over days post-implantation as these values remain consistent over time (figure 7(b, c)). Nor did decoding error seem to be explained by the baseline level of correlation between channels, which was significantly different between implants. More interestingly, session-to-session changes in the e-fold distance of up to 5 mm did not coincide with proportional changes in decoding error in the same implant. Instead, the non-monotonic relationship between decoding error and days post-implantation are at least partially explained by the number of electrode channels available on any given recording day; for example, the highest decoding error was seen on day 22 when there were only 32 channels recorded in animal one (figure 8(c), shown in black). After an interval that spanned day 9 to day 22, during which several channels were not recorded due to amplifier saturation, the error level resumed a gradual increase over time. (We addressed the saturation problem by adding a high-pass filter to the second version of the headstage, which increased the yield of functioning channels to 60 per day in the other animal). As a converse example, the decoding error was not strongly affected by the development of a highly correlated set of channels from days 20-45 in the other implanted array (animal two). In fact, the decoding performance degraded when these channels were excluded from the classification algorithm.

While large changes in the correlation length were likely related to electrical coupling, smaller week-to-week fluctuations in the correlation length (figure 4(d)) might be the effect of an evolving conductivity landscape caused by different tissue responses. For example, the build up of collagen (lower conductivity) and transient micro-hematomas (higher conductivity) are common in epidural implants of flexible electrode arrays [40]. In addition, the electrode array's surface geometry has been shown to influence the thickness of encapsulation tissue beneath the array [41], affecting both the electrode-electrolyte interface impedance [42] and the conductivity of the medium between the electrode and the neural sources [43]. For future electrode designs, we will consider alternate substrate geometries and materials that may increase the performance of the array.

5. Conclusion

These results indicate that our low-cost, multiplexed electrophysiological system can be used to record high-volume surface potentials from the primary auditory cortex and surrounding auditory areas in anesthetized rats, and also in freely-moving awake rats for a period of at least one month. In addition, we have developed a series of rigorous signal

characteristics for analyzing μECoG signals. These signal processing tools can be generalized to any local field potential recording. The high-resolution signal sensed by this array would be useful for μECoG-based BMI studies in rodents, which have been limited by low-resolution recording techniques. The present work represents a stride towards establishing reliable and accessible long-term recording from freely-moving animals. The use of such recordings is essential for studying dynamic processes such as learning during operant conditioning and studying plasticity mechanisms underlying perceptual and cognitive improvements during neuroprosthetic use.

Supplementary Material

Refer to Web version on PubMed Central for supplementary material.

Acknowledgements

We would like to thank Julia King for her assistance with implantation surgery and Ina Shehu for her assistance with the awake recordings. This work was funded by an NYU Postdoctoral and Transition Program for Academic Diversity Fellowship (M.N.I.); National Science Foundation award CCF-1422914 (M.J.T. and J.V.); Army Research Office award W911NF-14-1-0173 (C-H. C. and J.V.); NIDCD (DC009635 and DC012557), a Hirschl/Weill-Caulier Career Award, and a Sloan Research Fellowship (R.C.F.); and the NYU Grand Challenge Award (R.C.F. and J.V.).

References

1. Chang EF. Towards large-scale, human-based, mesoscopic neurotechnologies. Neuron. 2015; 86:68–78. [PubMed: 25856487]
2. Fukushima M, Chao ZC, Fujii N. Studying brain functions with mesoscopic measurements: Advances in electrocorticography for non-human primates. Curr. Opin. Neurobiol. 2015; 32:124–31. [PubMed: 25889531]
3. Fukushima M, Saunders RC, Mullarkey M, Doyle AM, Mishkin M, Fujii N. An electrocorticographic electrode array for simultaneous recording from medial, lateral, and intrasulcal surface of the cortex in macaque monkeys. J. Neurosci. Methods. 2014; 233:155–65. [PubMed: 24972186]
4. Bosman CA, Schoffelen J-M, Brunet N, Oostenveld R, Bastos AM, Womelsdorf T, Rubehn B, Stieglitz T, De Weerd P, Fries P. Attentional Stimulus Selection through Selective Synchronization between Monkey Visual Areas. Neuron. 2012; 75:875–88. [PubMed: 22958827]
5. Khodagholy D, Gelinas JN, Thesen T, Doyle W, Devinsky O, Malliaras GG, Buzsáki G. NeuroGrid : recording action potentials from the surface of the brain. Nat. Neurosci. 2014
6. Toda H, Suzuki T, Sawahata H, Majima K, Kamitani Y, Hasegawa I. Simultaneous recording of ECoG and intracortical neuronal activity using a flexible multichannel electrode-mesh in visual cortex. Neuroimage. 2011; 54:203–12. [PubMed: 20696254]
7. Slutzky MW, Jordan LR, Lindberg EW, Lindsay KE, Miller LE. Decoding the rat forelimb movement direction from epidural and intracortical field potentials. J. Neural Eng. 2011; 8:036013. [PubMed: 21508491]
8. Dimitriadis G, Fransen AMM, Maris E. Sensory and cognitive neurophysiology in rats, Part 1: Controlled tactile stimulation and micro-ECoG recordings in freely moving animals. J. Neurosci. Methods. 2014; 232:63–73. [PubMed: 24820913]
9. Richner TJ, Baumgartner R, Brodnick SK, Azimipour M, Krugner-higby LA, Eliceiri KW. Patterned optogenetic modulation of neurovascular and metabolic signals. J. Cereb. Blood Flow Metab. 2014; 35:140–7. [PubMed: 25388678]
10. Castagnola E, Maiolo L, Maggiolini E, Minotti A, Marrani M, Maita F, Pecora A, Angotzi GN, Ansaldo A, Boffini M, Fadiga L, Fortunato G, Ricci D. PEDOT-CNT-Coated Low-Impedance, Ultra-Flexible, and Brain-Conformable Micro-ECoG Arrays. IEEE Trans. neural Syst. Rehabil. Eng. a Publ. IEEE Eng. Med. Biol. Soc. 2015; 23:342–50.

11. Ledochowitsch P, Olivero E, Blanche T, Maharbiz MM. A transparent μECoG array for simultaneous recording and optogenetic stimulation. Conf. Proc. ... Annu. Int. Conf. IEEE Eng. Med. Biol. Soc. IEEE Eng. Med. Biol. Soc. Annu. Conf. 2011; 2011:2937–40.
12. Richner TJ, Thongpang S, Brodnick SK, Schendel A a, Falk RW, Krugner-Higby L a, Pashaie R, Williams JC. Optogenetic micro-electrocorticography for modulating and localizing cerebral cortex activity. J. Neural Eng. 2014; 11:016010. [PubMed: 24445482]
13. Viventi J, Kim D-H, Vigeland L, Frechette ES, Blanco JA, Kim Y-S, Avrin AE, Tiruvadi VR, Hwang S-W, Vanleer AC, Wulsin DF, Davis K, Gelber CE, Palmer L, Van der Spiegel J, Wu J, Xiao J, Huang Y, Contreras D, Rogers JA, Litt B. Flexible, foldable, actively multiplexed, high-density electrode array for mapping brain activity in vivo. Nat. Neurosci. 2011; 14:1599–605. [PubMed: 22081157]
14. Escabí MA, Read HL, Viventi J, Kim D-H, Higgins NC, Storace D a, Liu ASK, Gifford AM, Burke JF, Campisi M, Kim Y-S, Avrin AE, Spiegel Jan V Der, Huang Y, Li M, Wu J, Rogers JA, Litt B, Cohen YE. A high-density, high-channel count, multiplexed μECoG array for auditory-cortex recordings. J. Neurophysiol. 2014; 112:1566–83. [PubMed: 24920021]
15. Woods V, Wang C, Bossi S, Insanally M, Trumpis M, Froemke R, Viventi J. A low-cost, 61-channel μECoG array for use in rodents. 2015 7th International IEEE/EMBS Conference on Neural Engineering (NER). 2015:573–6.
16. Wang J, Trumpis M, Insanally M, Froemke R, Viventi J. A low-cost, multiplexed electrophysiology system for chronic μECoG recordings in rodents. 2014 36th Annual International Conference of the IEEE Engineering in Medicine and Biology Society (IEEE). 2014:5256–9.
17. Bink H, Wagenaar JB, Viventi J. Data acquisition system for high resolution, multiplexed electrode arrays. 2013 6th Int. IEEE/EMBS Conf. Neural Eng. 2013:1001–4.
18. Thomson DJ. Spectrum estimation and harmonic analysis. Proc. IEEE. 1982; 70:1055–96.
19. Pesaran B, Pezaris JS, Sahani M, Mitra PP, Andersen R a. Temporal structure in neuronal activity during working memory in macaque parietal cortex. Nat. Neurosci. 2002; 5:805–11. [PubMed: 12134152]
20. Harris KD, Henze DA, Csicsvari J, Hirase H, Buzsáki G. Accuracy of tetrode spike separation as determined by simultaneous intracellular and extracellular measurements. J. Neurophysiol. 2000; 84:401–14. [PubMed: 10899214]
21. Schmitzer-Torbert N, Jackson J, Henze D, Harris K, Redish AD. Quantitative measures of cluster quality for use in extracellular recordings. Neuroscience. 2005; 131:1–11. [PubMed: 15680687]
22. Blanco JA, Stead M, Krieger A, Viventi J, Marsh WR, Lee KH, Worrell GA, Litt B. Unsupervised classification of high-frequency oscillations in human neocortical epilepsy and control patients. J. Neurophysiol. 2010; 104:2900–12. [PubMed: 20810694]
23. Schalk G, Leuthardt EC, Brunner P, Ojemann JG, Gerhardt LA, Wolpaw JR. Real-time detection of event-related brain activity. Neuroimage. 2008; 43:245–9. [PubMed: 18718544]
24. Ziskind AJ, Emondi AA, Kurgansky AV, Rebrik SP, Miller KD. Neurons in cat V1 show significant clustering by degree of tuning. J. Neurophysiol. 2015; 113:2555–81. [PubMed: 25652921]
25. Ledoit O, Wolf M. A well-conditioned estimator for large-dimensional covariance matrices. J. Multivar. Anal. 2004; 88:365–411.
26. Destexhe A, Contreras D, Steriade M. Spatiotemporal analysis of local field potentials and unit discharges in cat cerebral cortex during natural wake and sleep states. J. Neurosci. 1999; 19:4595–608. [PubMed: 10341257]
27. Gelfand, AE. Handbook of spatial statistics. CRC Press; Boca Raton: 2010.
28. Smith E, Kellis S, House P, Greger B. Decoding stimulus identity from multi-unit activity and local field potentials along the ventral auditory stream in the awake primate: implications for cortical neural prostheses. J. Neural Eng. 2013; 10:016010. [PubMed: 23283406]
29. Schwartz RS, Brown EN, Lydic R, Schiff ND. General anesthesia, sleep, and coma. N. Engl. J. Med. 2010; 363:2638–50. [PubMed: 21190458]
30. Polley DB, Read HL, Storace DA, Merzenich MM. Multiparametric auditory receptive field organization across five cortical fields in the albino rat. J. Neurophysiol. 2007; 97:3621–38. [PubMed: 17376842]

31. Insanally MN, Kover H, Kim H, Bao S. Feature-Dependent Sensitive Periods in the Development of Complex Sound Representation. J. Neurosci. 2009; 29:5456–62. [PubMed: 19403813]
32. Hromádka T, DeWeese MR, Zador AM. Sparse representation of sounds in the unanesthetized auditory cortex. PLoS Biol. 2008; 6:e16. others. [PubMed: 18232737]
33. Gaese BH, Ostwald J. Anesthesia changes frequency tuning of neurons in the rat primary auditory cortex. J. Neurophysiol. 2001; 86:1062–6. [PubMed: 11495976]
34. Kisley MA, Gerstein GL. Trial-to-trial variability and state-dependent modulation of auditory-evoked responses in cortex. J. Neurosci. 1999; 19:10451–60. [PubMed: 10575042]
35. Ter-Mikaelian M, Sanes DH, Semple MN. Transformation of Temporal Properties between Auditory Midbrain and Cortex in the Awake Mongolian Gerbil. J. Neurosci. 2007; 27:6091–102. [PubMed: 17553982]
36. NeuroNexus Technologies. NeuroNexus 2015 Research Product Catalog. 2015
37. Henle C, Schuettler M, Ordonez JS, Stieglitz T. Scaling limitations of laser-fabricated nerve electrode arrays. Conf. Proc. IEEE Eng. Med. Biol. Soc. 20082008:4208–11. [PubMed: 19163640]
38. Henle C, Raab M, Cordeiro JG, Doostkam S, Schulze-Bonhage A, Stieglitz T, Rickert J. First long term in vivo study on subdurally implanted Micro-ECoG electrodes, manufactured with a novel laser technology. Biomed. Microdevices. 2011; 13:59–68. [PubMed: 20838900]
39. Kohler F, Schuettler M, Ordonez J, Stieglitz T. Laser Microfabrication of Neural Electrode Arrays: Comparison of Nanosecond and Picosecond Laser Technology. Proc. IFESS. 2011; 102:99–101.
40. Schendel AA, Thongpang S, Brodnick SK, Richner TJ, Lindevig BDB, Krugner-Higby L, Williams JC. A cranial window imaging method for monitoring vascular growth around chronically implanted micro-ECoG devices. J. Neurosci. Methods. 2013; 218:121–30. [PubMed: 23769960]
41. Schendel AA, Nonte MW, Vokoun C, Richner TJ, Brodnick SK, Atry F, Frye S, Bostrom P, Pashaie R, Thongpang S, Eliceiri KW, Williams JC. The effect of micro-ECoG substrate footprint on the meningeal tissue response. J. Neural Eng. 2014; 11:046011. [PubMed: 24941335]
42. Merrill DR, Tresco P a. Impedance characterization of microarray recording electrodes in vitro. IEEE Trans. Biomed. Eng. 2005; 52:1960–5. [PubMed: 16285400]
43. Grill WM, Mortimer JT. Electrical properties of implant encapsulation tissue. Ann. Biomed. Eng. 1994; 22:23–33. [PubMed: 8060024]

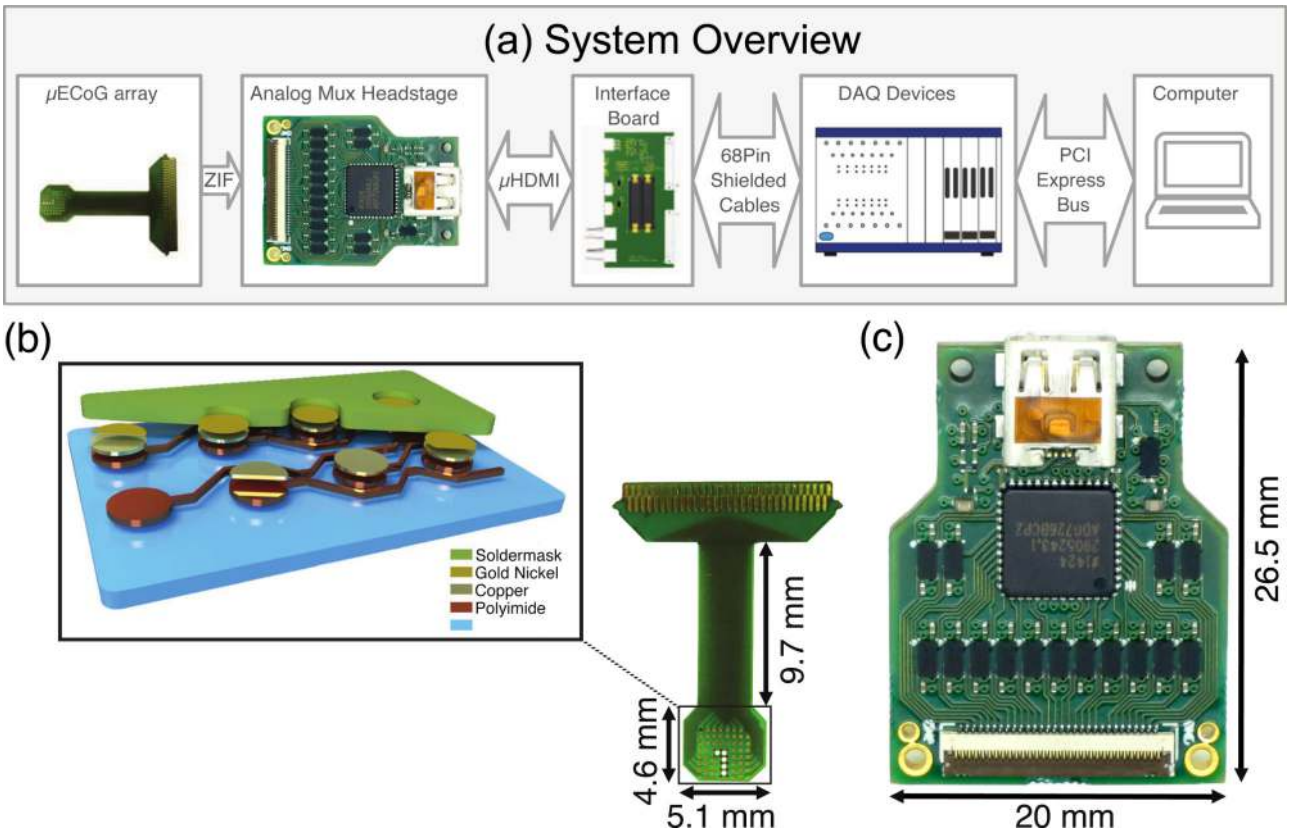

Figure 1.

A low cost, 60-channel analog multiplexed electrophysiology system. (a) The design included unity gain buffering, multiplexing, amplification and filtering in a small form factor. The μECoG system was connected via μHDMI to a National Instruments multicard PXI data acquisition system and data were recorded on a laptop computer. (b) The electrode array had 61 contacts that were 203 μm in diameter and spaced 406 μm apart. The dark electrode in the upper left hand corner of the array was intentionally not exposed to test the encapsulation material. Five laser cut holes (305 μm in diameter) are included to provide access for intracortical electrodes. The 3D cross sectional schematic of the electrode array shows the material composition. The actual layers thicknesses of the electrode arrays are the following: Soldermask: 15 μm, Gold: 0.125 μm, Nickel: 3 μm, Copper: 5 μm, Polyimide: 12 μm. The total thickness is ~30 μm. (c) Each side of the headstage system included 15 dual op-amps configured as buffers, a dual 16:1 multiplexer and a dual op-amp to provide 20× gain (the front side with a 61-pin ZIF connector is shown, the back side contains another set of the same circuits).

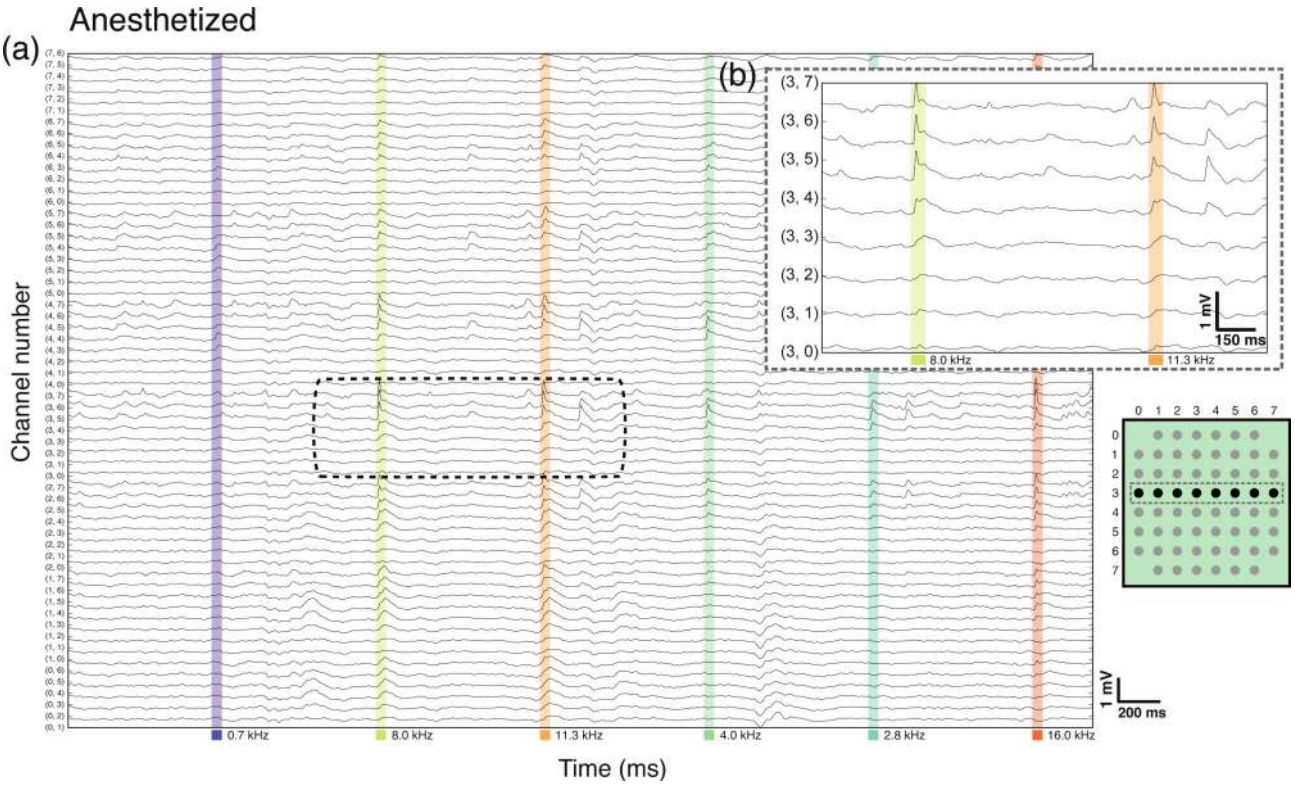

Figure 2.

Continuous μECoG recording from an anesthetized animal under pentobarbital. (a) In vivo μECoG recording of single trial auditory evoked activity demonstrated high quality electrophysiology from the recording system. All 60 channels from the μECoG array are shown. An auditory stimulus was presented at the times indicated by the colored bars below the time axis. (b) Channels from the third row of the electrode are expanded to highlight the clear, single trial auditory evoked responses visible approximately 15 ms after stimulus onset. Ongoing background activity can also be observed.

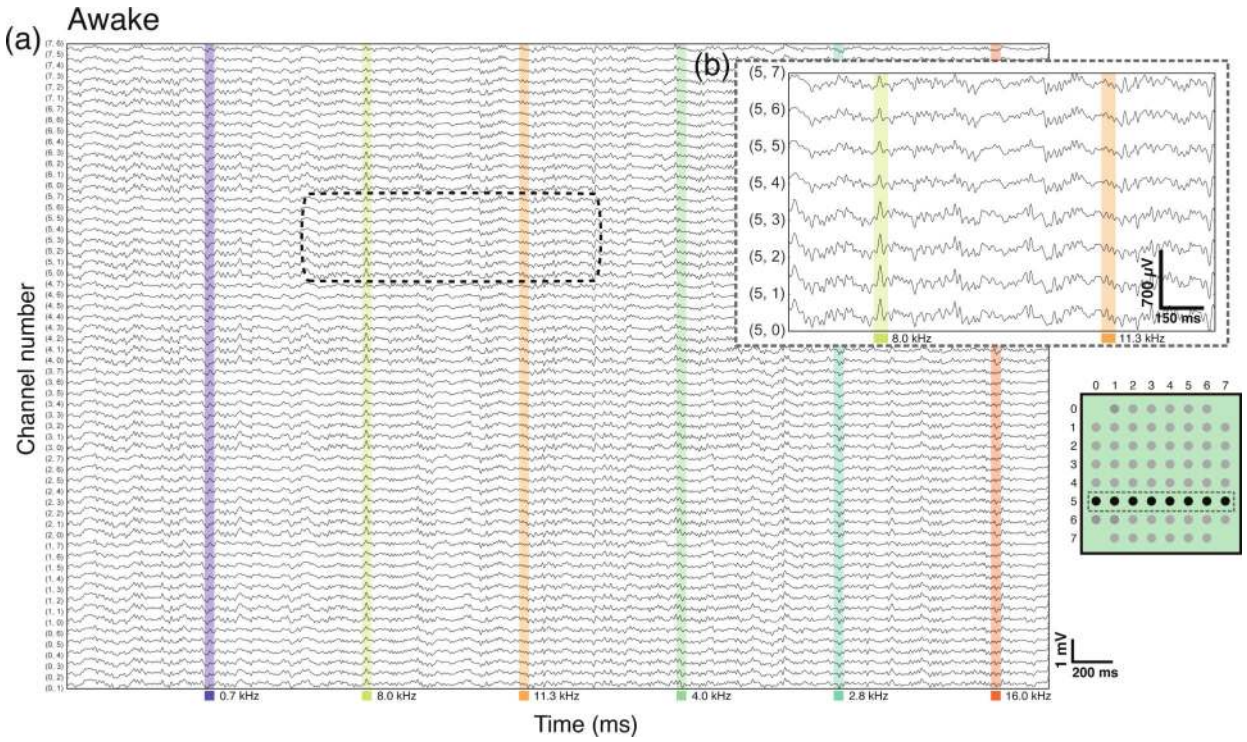

Figure 3.

Continuous μECoG recording from a freely moving animal. (a) Ongoing μECoG is shown on all 60 channels. All figure elements mirror figure 2. (b) Channels from the fifth row of the electrode are expanded to highlight an evoked response to an 8 kHz tone. Although background signal power was higher in the awake animal, single-trial evoked responses were still apparent.

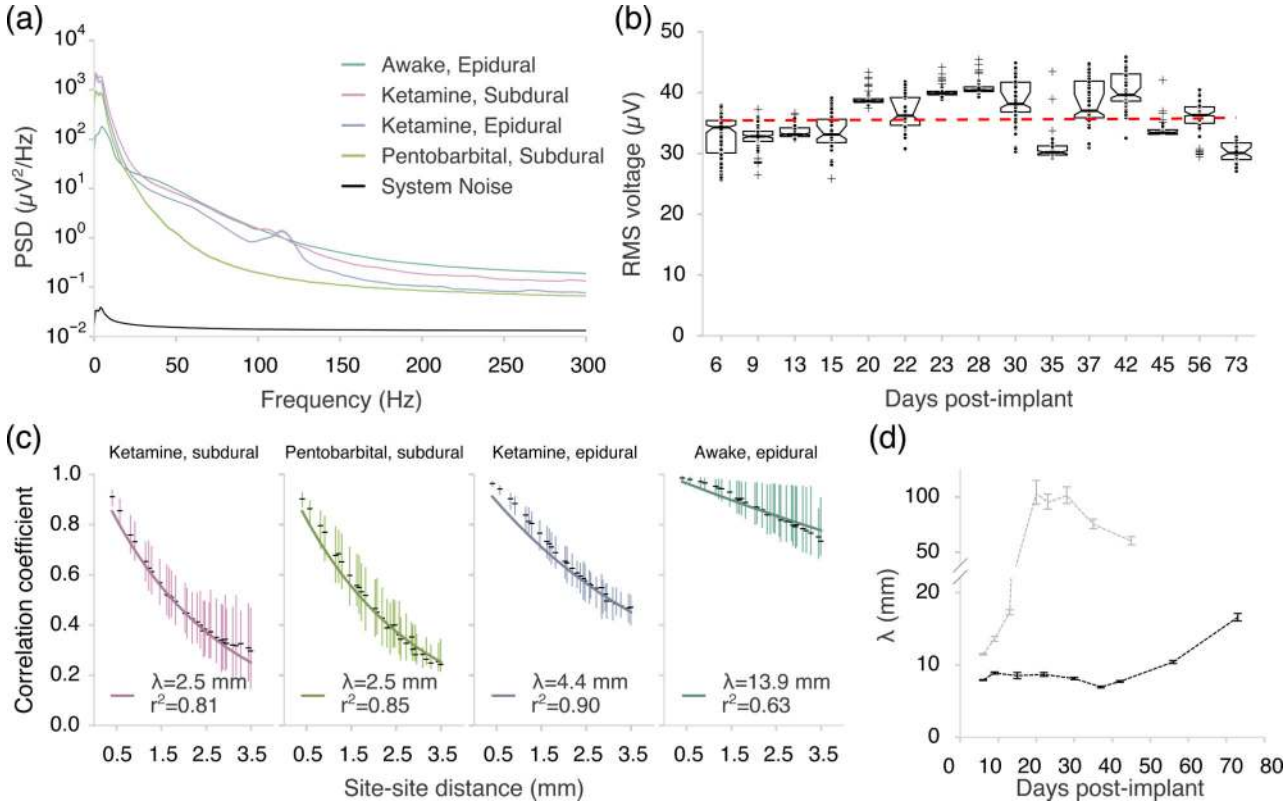

Figure 4.

Signal characteristics from anesthetized and awake recordings. (a) Power spectral densities of baseline (non-stimulated) μECoG for different experimental conditions (mean ± S.E.M). Noise measurements were taken from an electrode in saline and reflect the total system noise of the headstage electronics and the thermal noise of the electrode. Number of sites per group: awake, epidural=861 (17 recordings), ketamine, subdural=300 (5 recordings), ketamine, epidural=240 (4 recordings), pentobarbital, subdural=120 (2 recordings), and system noise=60 (1 recording). (b) RMS voltage in the 10-100 Hz band for awake recording sessions in two animals spanning 10 weeks. The dashed line indicates the linear regression (slope 0.01 μV/day, $p>0.05$). Number of sites per day: day 6=108 (48+60, n=2), day 9=110 (50+60, n=2), day 13=60, day 15=39, day20=58, day 22=35, day 23=60, day 28=60, day 30=60, day 35=60, day 37=60, day 42=52, day 45=60, day 56=60, day 73=53. (c) Spatial correlation profiles for four *in vivo* recording conditions. Vertical lines span the interquartile range of the distribution of correlation per distance and black dashes represent the medians. The number of site-site pairs per group is: ketamine, subdural=8,732, pentobarbital, subdural=3,540, ketamine, epidural=7,080, awake, epidural=23869. (d) *e*-fold distance for awake recording sessions spanning up to 10 weeks (n=2).

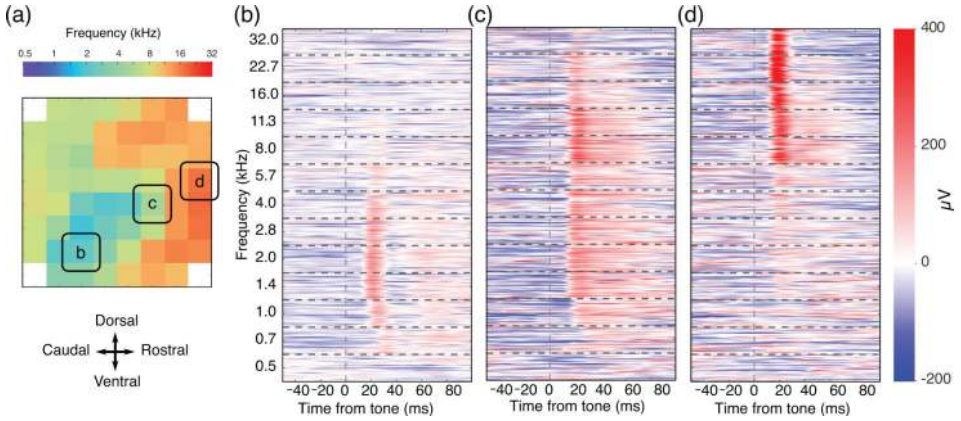

Figure 5.

Best frequency map and high trial-to-trial reliability of evoked responses under pentobarbital anesthesia. (a) Best frequency for each channel is rendered as a map over the recorded area for 70 dB SPL tones. (b), (c) and (d) The responses for 390 trials are ordered by tone and stacked for the three channels highlighted in the best frequency map. The smooth ridges and valleys of the voltage heat map depict high trial-to-trial reliability in the response waveform to each tone.

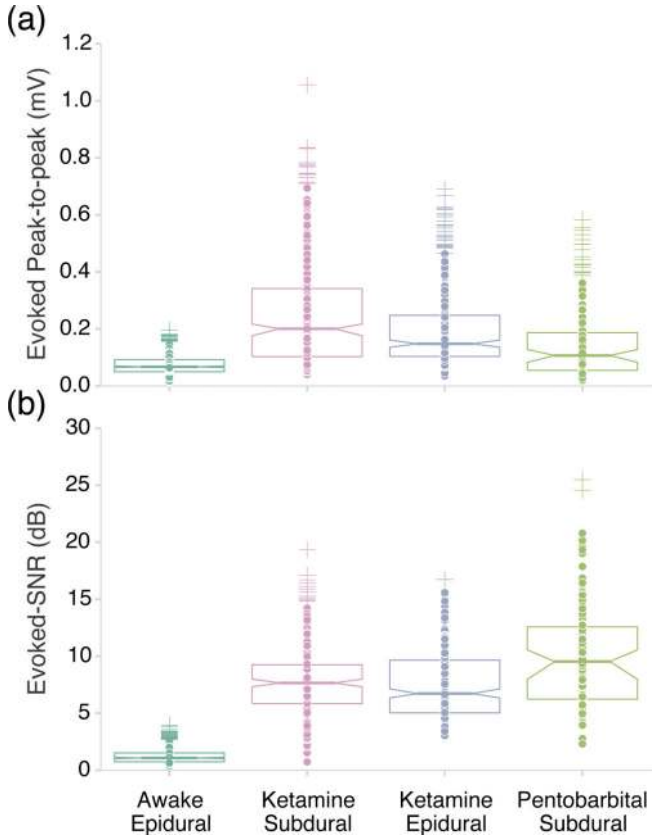

Figure 6.

Tone-evoked response scores of electrode sites at best frequency for different experimental conditions. (a) Evoked peak-to-peak amplitudes averaged over trials under awake epidural (83.7 μV), ketamine subdural (200 μV), ketamine epidural (148 μV), and pentobarbital subdural (107 μV). Each dot represents an electrode site. (b) Evoked SNR for different experimental conditions. Number of sites per group: awake, epidural=665 (17 recordings), ketamine, subdural=460 (9 recordings), ketamine, epidural=316 (5 recordings), pentobarbital, subdural=156 (3 recordings).

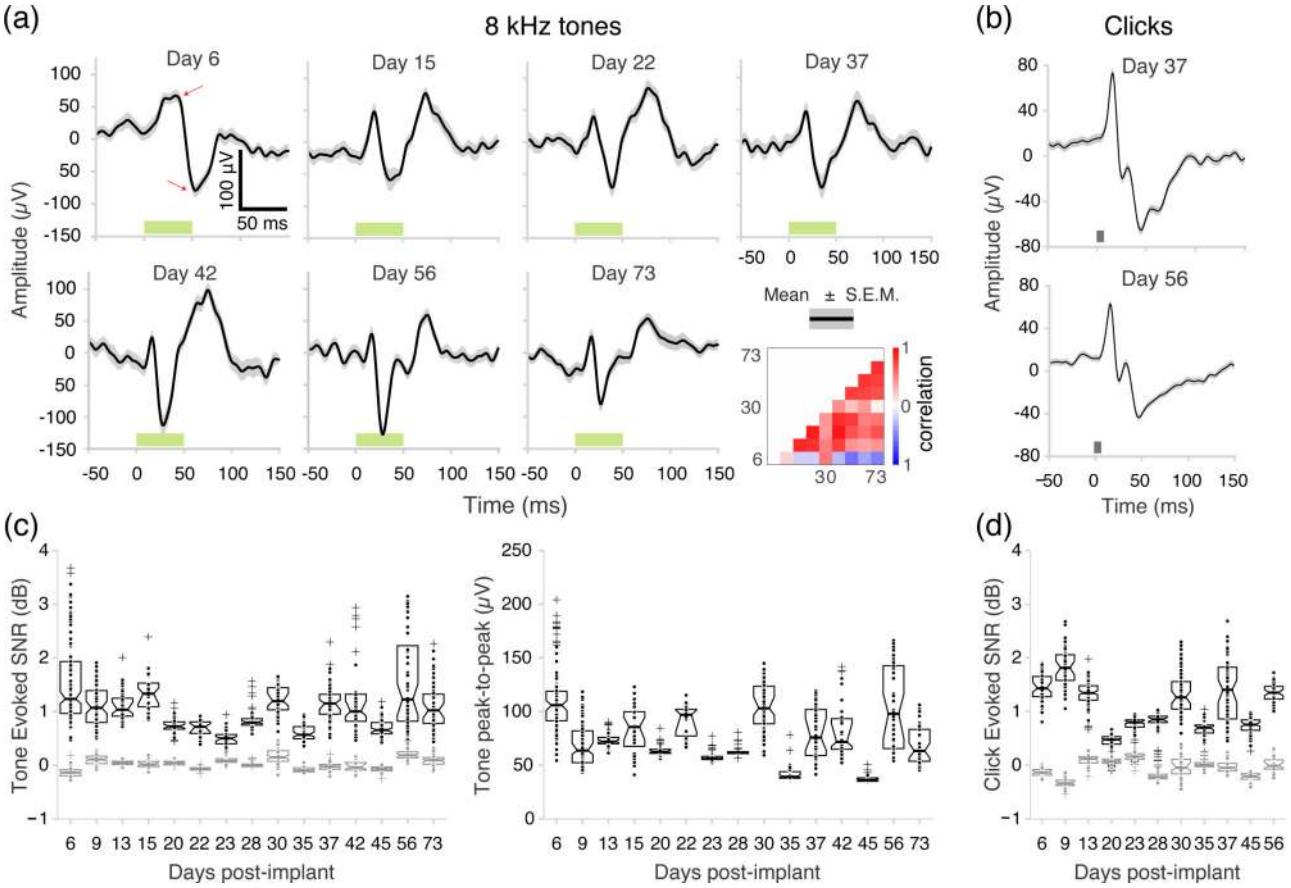

Figure 7.

Evoked responses recorded from a freely-moving animal. (a) Examples of evoked response waveforms to 8 kHz pure tones at 70 dB SPL from the same electrode over 10 weeks. The dark grey line represents the average evoked response to 8 kHz over 30 trials and the light gray shading represents the S.E.M. Green bars represent stimulus duration. (b) Examples of click evoked responses from a single recording site from day 37 post-implantation (*top*), and from day 56 post-implantation (*bottom*). Grey bars represent stimulus duration. (c) *Left*, Evoked SNR for the best frequency tone at 70 dB SPL over awake recording sessions (n=2 animals). Control SNR scores (grey) were computed by replacing response vectors with a set of interstimulus baseline that was distinct from the reference baseline sample. *Right,* Peak-to-peak response amplitude for the best frequency tone at 70 dB SPL across awake recording sessions (n=2 animals). The red arrows in (a) show how the peak-to-peak amplitudes were measured. Number of channels with pure tone responses: day 6=108 (48+60, n=2), day 9=107 (49+58, n=2), day 13=60, day 15=32, day 20=58, day 22=23, day 23=60, day 28=60, day 30=60, day 35=60, day 37=50, day 42=35, day 45=54, day 56=59, day 73=53. (d) Evoked SNR scores for click stimuli for 11 awake recording sessions. Black dots represent individual channels. All 60 channels responded to clicks for each session in (d).

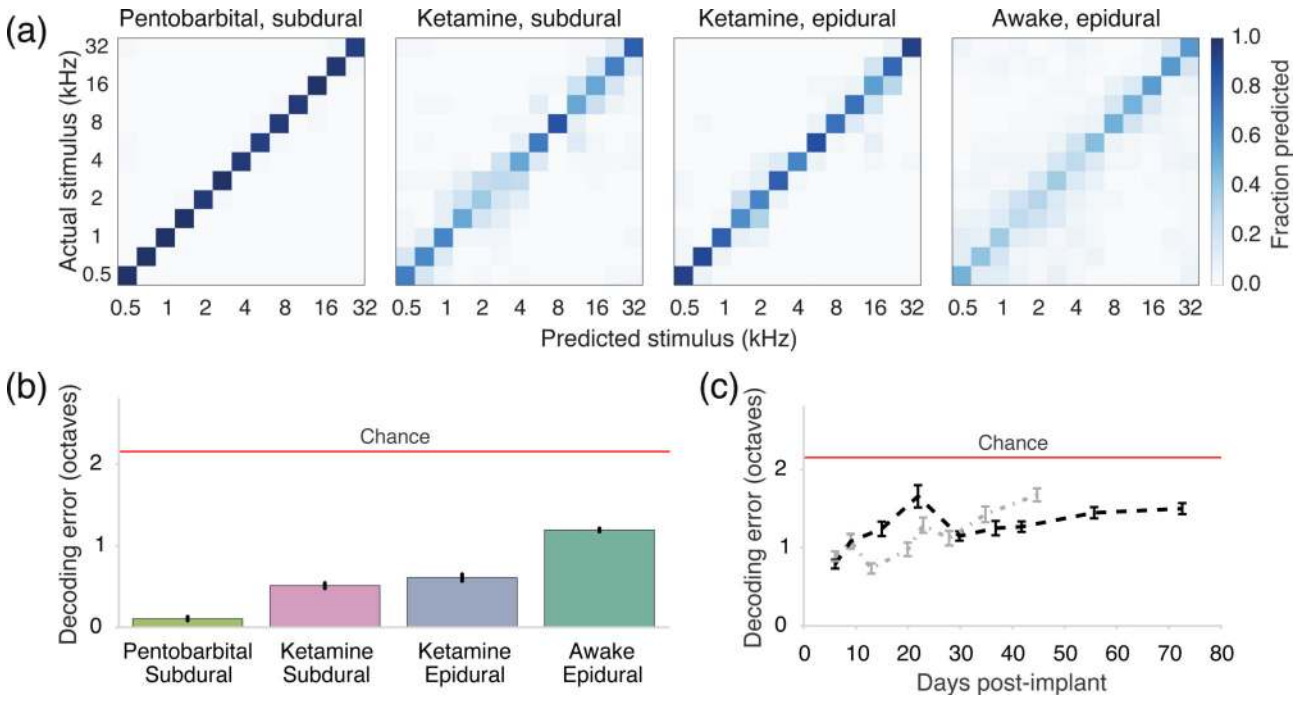

Figure 8.

Tone decoding results from anesthetized and awake recordings. (a) Confusion matrices were computed for linear classifier performance over 6-fold cross-validation for the highest-accuracy recordings from each experimental condition (ketamine epidural=77%, ketamine subdural=60%, pentobarbital subdural=98%, and awake epidural= 41%). (b) Decoding error was 0.11 octaves for the pentobarbital subdural (3 recordings from n=2 animals), 0.53 and 0.65 octaves under ketamine (8 subdural recordings from n=4 animals and 6 epidural recordings from n=3 animals respectively), and the average performance of awake epidural recordings showed an error of 1.2 octaves (17 recordings from n=2 animals). Red line represents chance. (c) Decoding error was tracked up to ten weeks in two freely moving animals (black and grey dashed lines). The 95% confidence intervals of decoding error in (b) and (c) were estimated from 10000 bootstrap replicates of the confusion matrices for each group of recordings.